An Adaptive Power System Equivalent for Real-Time Estimation of Stability Margin Using Phase-Plane Trajectories

Kai Sun, *Member, IEEE*, Stephen T. Lee, *Senior Member, IEEE*, and Pei Zhang, *Senior Member, IEEE*

***Abstract*—This paper studies real-time estimation of stability margin of a power system under disturbances by continuous measurement data. The paper presents a ball-on-concave-surface (BOCS) mechanics system as a power system's adaptive equivalent representing its real-time status and the stability region about a monitored variable. The parameters of the equivalent are adaptive to the operating condition and can online be identified from the phase-plane trajectories of the monitored variable. Accordingly, the stability margin and risk of instability can be estimated. Case studies on a two-generator system and a 179-bus system show that the BOCS system can be applied either locally or for wide-area stability monitoring in real-time calculation of stability margin. This paper proposes a new idea for using real-time measurements to develop and identify a power system's adaptive equivalent as a basis for online prediction of instability.**

***Index Terms*—Ball-on-concave-surface system, logarithmic spiral, phase-plane trajectory, phasor measurement unit, stability margin, synchrophasor, transient stability, wide-area monitoring.**

I. Introduction

EARLY indication of impending instability in a power system under disturbance conditions is vitally important for prevention of major power outages. While a series of disturbances are increasingly stressing the system, degradation of its stability margin may finally lead to loss of stability. Computer simulations that are performed beforehand on assumed contingencies may not help correctly foresee potential instability in real time if the happening disturbances do not exactly match simulated contingencies or the operating condition has been different from what is concerned in simulations. Increasingly installed synchrophasors, e.g., phasor measurement units (PMUs), can continuously provide high-sampling-rate and synchronized phasor measurements over wide areas, which are ideal in monitoring dynamic behaviors of a power system in real time. Some researches have focused on tying real-time phasor measurements with pre-existing knowledge (e.g., on what variables are good indicators of instability and what their thresholds are) obtained from computer simulation results or historical events to enable real-time stability assessment or prediction under disturbance conditions [1]–[5]. Other efforts utilize real-time phasor measurements taken at strategically selected locations to directly monitor inter-area oscillation modes or computed energy functions for potential small-signal instability or transient instability [6]–[8].

When a power system is continuously impacted by a series of disturbances, its increasing weakness is reflected by growing swings among generators, which can be detected in real time from measurements at multiple locations. This paper proposes a new method for real-time calculation of stability margin only using continuous high-sampling-rate measurements. The proposed method employs a mechanics system as a power system equivalent, which is a ball rolling on a concave surface, respectively, representing the real-time system status and stability region in terms of a monitored variable, e.g., frequency, bus voltage magnitude, rotor angle difference, or stability index defined for a wide area. Continuous measurements on the variable at a high sampling rate enable authentically presenting its phase-plane trajectories under disturbances, by which the parameters of that equivalent are estimated. Then, stability margin and instability risk indices are calculated from the location of the ball relative to the surface. The method can be applied to either a local variable by an independent measurement device or a wide-area stability index (e.g., the average angle difference between two interconnected areas) calculated using phasor measurements. This paper will focus on validating the idea of the proposed method and study its potentials in local and wide-area applications.

The rest of the paper is organized as follows. Section II first proposes the adaptive power system equivalent—BOCS system. Then, real-time estimation of its parameters and stability margin by measurement data will be introduced. Section III performs case studies on a two-generator system and a 179-bus test system. Finally, Section IV gives conclusions and points out future work.

II. Proposed Method

A. Ball-on-Concave-Surface System

Disturbances on a power system will cause generators to swing, which can clearly be reflected from the measurements at extensive locations. Select a system variable to monitor. Following a disturbance, damped swings in the variable's value indicate the stabilization process of the system and can be visualized by its phase-plane trajectory. A study in [9] shows that unstable or marginally stable phase-plane trajectories (indicating negative or insufficient stability margin) are qualitatively identifiable by pattern recognition technologies. This paper studies the quantitative relationship between the stability margin and parameters of a phase-plane trajectory.

Manuscript received March 18, 2010; revised May 12, 2010; accepted June 18, 2010. Date of publication August 03, 2010; date of current version April 22, 2011. This work was supported by the Electric Power Research Institute (EPRI). Paper no. TPWRS-00213-2010.

The authors are with EPRI, Palo Alto, CA 95134 USA (e-mail: ksun@epri.com; slee@epri.com; pzhang@epri.com).

Color versions of one or more of the figures in this paper are available online at http://ieeexplore.ieee.org.

Digital Object Identifier 10.1109/TPWRS.2010.2055900

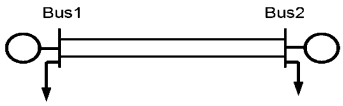

Fig. 1. Two-generator power system.

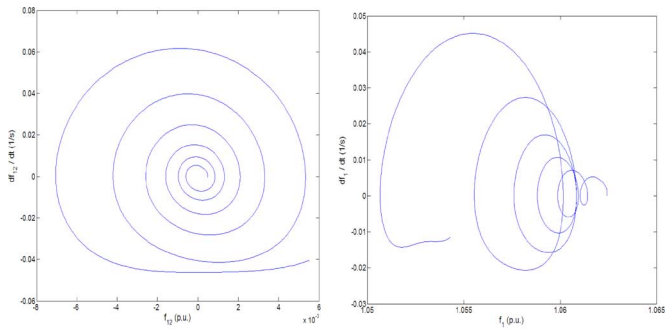

(a) (b)

Fig. 2. Stable phase trajectories.

Consider a power system with two generators as shown in Fig. 1 and add a temporary short-circuit fault at bus 1. Fig. 2 gives the phase-plane trajectory of frequency difference f_{12} between generators 1 and 2 following the fault and the phase-plane trajectory of frequency f_1 of generator 1. Both trajectories have spiral-like patterns with decreasing swings indicating stabilization of the system after the fault.

As shown in Fig. 3, consider an analogy between a monitored variable's phase-plane trajectory under disturbances and the trajectory of a ball rolling on a 3-D concave surface in a gravitational field g. It seems that trajectories in Fig. 2(a) and (b) are, respectively, seen from viewpoint A and viewpoint B in Fig. 3. Thus, we define such a ball-on-concave-surface (BOCS) system as a power system equivalent about the monitored variable. At any time, the surface is concave within a certain boundary, in which the stability region of that variable is represented. The ball has a stable equilibrium point at the surface's bottom representing the variable's steady-state value. The BOCS system, in fact, represents a projection of the original high-dimensional power system onto a 3-D Euclidean space depending on the monitored variable. The parameters of the BOCS system are adaptive to the operating condition and can be online identified using the monitored variable's phase-plane trajectory obtained from its high-sampling-rate measurements. Theoretically, only if the monitored variable itself is able to detect Lyapunov instability of the original power system, the resulted BOCS system is effective in providing credible trending information on stability margin and correctly detecting zero margin when the system loses stability. Some variables might not create an effective high-dimension-to-3-D projection to help detect instability. For instance, if the system has multiple areas going to lose synchronism due to disturbances, a single system variable within one area (e.g., one generator angle) may not detect that instability.

Although the monitored variable is important to the performance of the proposed method, it is not hard to select by means of the knowledge on the concerned stability problem and engineering judgment. Generally speaking, potentially unstable system variables are good candidates for monitoring and the basis of identifying a BOCS system. To monitor a wide-area stability problem, e.g., potential angular instability between two interconnected areas, two types of candidates for the monitored variable are

- the angle/frequency difference between the two areas;
- the variables at their interface.

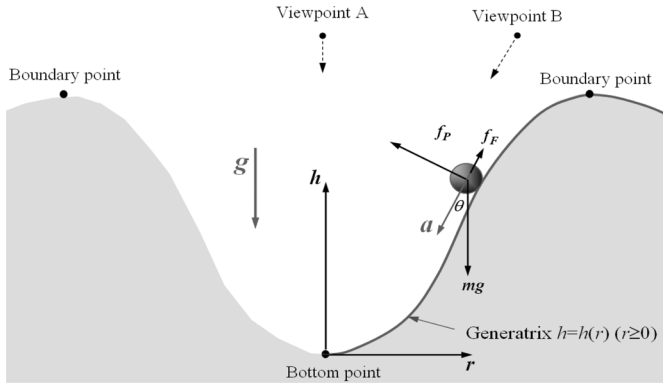

Fig. 3. Ball-on-concave-surface system as a power system equivalent.

Based on a certain variable, the estimated concave surface may change its shape under different operating conditions in terms of network topology and power flows. Ignore its changes under one operating condition and describe it by a time-variant (in fact, piecewise time-invariant) 3-D surface function:

$$z = F(x, y, t) = \bar{F}_k(x, y), \quad t_k < t < t_{k+1} \tag{1}$$

where $t_k \sim t_{k+1}$ is the period for one operating condition. Once the operating condition changes due to a disturbance or control action, $\bar{F}_k$ is switched to $\bar{F}_{k+1}$. About each time-invariant function $\bar{F}_k$, assume:

- the boundary of keeping concavity is a closed curve consisting of continuous ridge points, named boundary points, where a principal curvature reaches its extremum;
- within the boundary, $\bar{F}_k$ is differentiable and has one minimum (i.e., the bottom point).

Stressing the operating condition (e.g., weaken the network topology) may shrink the boundary of the concave surface to give the ball a higher risk of going outside, i.e., the system losing stability. For a temporary fault without changing the operating condition, pre- and post-fault surfaces are identical, but the ball is activated with an amount of energy (depending on the fault duration) to move on the surface. Disturbances with temporary and permanent faults will, respectively, be considered by two case studies in Section III.

B. Estimation of the Surface Function

This paper will focus on approximating $F\ (x, y, t)$ by a special type of $\bar{F}_k$, which is a surface of revolution created by rotating a 2-D smooth curve, i.e., the generatrix, around the vertical axis. As shown in Fig. 3, regard the bottom point of the surface as origin (0, 0) and represent the generatrix by differentiable function $h = h(r)(r \geq 0)$, which has a stationary point at the origin. h and r, respectively, describe the vertical and horizontal locations (i.e., the height and trajectory radius) of the ball relative to the bottom point. The boundary point on the generatrix is denoted by (r_M, h_M), which is also a stationary point of $h(r)$, where h reaches its local maximum h_M.

At a location (r, h), the ball is subject to the following two mechanics equations in the directions, respectively, normal to the surface and parallel with the generatrix:

$$\begin{cases} mg\sin\theta + m\omega^2 r\cos\theta = f_P \\ mg\cos\theta - m\omega^2 r\sin\theta - f_F = ma = mv' \end{cases} \tag{2}$$

where m denotes the ball's mass, θ is the angle between h axis and the tangent, ω is its angular velocity around h axis, a and v are, respectively, the magnitudes of its acceleration and speed components that are tangent to the generatrix and towards the bottom, and f_P is the force given by the surface in the normal direction. There is also friction opposite to the ball's moving direction. f_F denotes the friction component tangent to the generatrix and is ignored in this paper.

Under disturbances, the multiple-generator system's dynamics behavior is influenced by multiple "forces". However, there is always one "force" being dominant over the others at least for a short time window (e.g., a few seconds). Gravity g with the proposed BOCS system corresponds to the currently dominant "force" and is assumed to keep constant over the time window. As indicated by the case study in Section III-A, with different values assumed for g, the concave surfaces inferred from the same phase-plane trajectory are only different in their vertical scales and indicate the same horizontal boundary, i.e., r_M. Hence, g taking different values in a time window does not affect detecting instability or predicting the trend towards instability. For each current time window, the proposed method aims at estimating how close the ball has been to the concave surface's boundary (under the effect of the dominant "force"), such that stability margin and instability risk indices in percentage can be computed online. Therefore, it is not necessary to accurately estimate g. We can either simply assume g to be a constant or estimate its value for each time window using (4) below. Considering that $h\ (r)$ may have a point $(r_0, h_0)(0 < r_0 < r_M)$ where the ball has its maximum speed, i.e., $v' = 0$, assume $\theta = \theta_0$ at (r_0, h_0) and derive (3) from (2):

$$g = \omega^2 r_0 \tan\theta_0. \tag{3}$$

Inspired by (3), g may take g_0 calculated for each time window:

$$g = g_0 = \bar{\omega}^2 \hat{r}_0 \tag{4}$$

where $\bar{\omega}$ is the average ω and $\hat{r}_0$, as an estimate of r_0, is r where $|v|$ reaches its maximum in the time window. An advantage of g taking g_0 is that if the operating condition is unchanged, estimates of $h(r)$ from different time windows will be close in shape since they have the same r_M and close values of θ_0 around $\pi/4$ from the comparison between (3) and (4).

With g available, the formula for estimating θ is derived as follows. Since r and v satisfy

$$v\sin\theta = -r' \tag{5}$$

take time derivatives of both sides of (5):

$$a\sin\theta + v\cos\theta\cdot\theta' = -r''. \tag{6}$$

Eliminate v in (5) and (6) to obtain (7):

$$a = -\frac{r''}{\sin\theta} + \frac{r'\theta'}{\tan\theta\sin\theta}. \tag{7}$$

Following a disturbance, the monitored variable's high-sampling-rate measurements over a time window are obtained and denoted by time series $x\,(t)$. A phase-plane trajectory about the variable can be plotted. How to estimate time series $\omega(t)$ and $r(t)$ using that phase-plane trajectory will be discussed later in Sections II-C and D. For any time t in the time window, with $\omega(t)$ and $r(t)$ available, $\theta(t)$ is determined by (2) and (7) and can be directly solved from them. The recursive equation shown in (8) at the bottom of the page provides an alternative approach, which is easier to implement. For concision, "t" with r and ω is omitted in (8). θ'_{k-1} is the time derivative of θ_{k-1}, and estimated using the values of θ_{k-1} around t. $\theta(t) \in [0, \pi/2]$ when $r(t) \in [0, r_M]$. Initial value $\theta_1(t)$ may take $\pi/4$. Recursively calculate (8) until $|\theta_k - \theta_{k-1}|/|\theta_k|$ is small enough, e.g., $<1\%$ to obtain an estimate of $\theta(t)$.

Over the time window, the estimated values of $\theta(t)$ are synchronized with the estimated values of $r(t)$ by means of time stamp "t". A function $\theta(r)$ can be inferred by eliminating "t" of $\theta(t)$ and $r(t)$. If multiple values of $\theta(t)$ (perhaps at multiple locations on the surface) corresponds to the same value of $r(t)$, average them to obtain the estimate of $\theta(r)$.

Let r_m be the maximum r over the time window. Because

$$\frac{dh}{dr} = \frac{1}{\tan\theta(r)} \tag{9}$$

function $h(r)$ for $r < r_m$ can be estimated by the following integral:

$$h(r) = \int_0^r \frac{dr}{\tan\theta(r)}, r < r_m. \tag{10}$$

In the following subsections, the approaches to estimating $r(t)$ and $\omega(t)$ over a time window are given, and the proposed BOCS-based method for computing stability margin and instability risk indices are presented as well as its flow chart.

C. Estimation of Radius r

Two approaches are proposed to estimate $r(t)$ from a phase-plane trajectory over a time window of T.

1) Logarithmic Spiral Fitting (LSF) Approach: At time $t = t_0$, use $x(t)$ to denote the monitored variable's measurements for time window $[t_0 - T, t_0]$, and ω_d and σ are, respectively, estimates of the angular frequency and damping coefficient of its dominant oscillation mode. There is

$$\begin{aligned} x(t) &= x_0 + Ae^{-\sigma t}\cos(\omega_d t + \theta_0) + \tilde{x}(t) \\ t &\in [t_0 - T, t_0] \end{aligned} \tag{11}$$

$$\theta_k = \left[\pi - \arcsin\left(\frac{\omega^2 r - 2r'' + 2r'\theta'_{k-1}/\tan\theta_{k-1}}{\sqrt{g^2 + \omega^4 r^2}}\right) - \arctan\left(\frac{\omega^2 r}{g}\right)\right] \Big/ 2 \tag{8}$$

where x_0 is the steady-state value of $x(t)$ and $\tilde{x}(t)$ is the signal with the other oscillation modes. Take time derivatives of both sides of (11):

$$x'(t) = -\lambda A e^{-\sigma t}\sin(\omega_d t + \theta_0 + \varphi) + \tilde{x}'(t) \tag{12}$$

where $\varphi = \arctan(\sigma/\omega_d)$ and $\lambda = \sqrt{\sigma^2 + \omega_d^2}$. There are two ways to estimate λ. One is to apply prony analysis to $x(t)$ of the current time window to estimate σ and ω_d, and then calculate λ. ω_d can also be approximated by $\bar{\omega}$ in (4). Another approximate but simpler way is to calculate the variances of $x(t)$ and $x'(t)$ over the time window and then adopt (13) to estimate λ:

$$\lambda \approx \sqrt{\mathrm{var}(x(t))/\mathrm{var}(x'(t))}. \tag{13}$$

Then calculate

$$y(t) = x'(t)/\lambda. \tag{14}$$

From (12)

$$y(t) = -Ae^{-\sigma t}\sin(\omega_d t + \theta_0 + \varphi) + \tilde{x}'(t)/\lambda. \tag{15}$$

In fact, $-\sigma \pm j\omega_d$ are a pair of approximate dominant poles for the current time window, and λ is their distance to the origin. When the system's stability margin decreases, the dominant poles will approach y axis. As a result, $|\varphi|$ will decrease. Thus, (11) and (15) are close to the following equations:

$$\begin{cases} x(t) = x_0 + Ae^{-\sigma t}\cos(\omega_d t + \theta_0) \\ y(t) = -Ae^{-\sigma t}\sin(\omega_d t + \theta_0) \end{cases} \tag{16}$$

which represent a clockwise logarithmic spiral with the center on x axis. Hence, $Ae^{-\sigma t}$ is an estimate of $r(t)$ and can be obtained by fitting the spiral to the trajectory described by (11) and (15). Reference [10] provides an algorithm for solving a logarithmic spiral that optimally fits a given spiral-like curve. Tests on the algorithm show that its result is insensitive to the drifting of λ, so approximate formula (13) can be used here.

The dominant oscillation mode ω_d may change with time windows of T because of the nonlinear nature of the multi-generator system. However, if there is always $T > 4\pi/\omega_d$ and the LSF approach is applied continuously, it can estimate r, adapting to the changes in mode dominance. For instance, if a trajectory switches its dominant mode from 0.2 Hz over a time window to 0.5 Hz over the next time window, the LSP approach with $T > 10$ s can capture that change by linking two spiral segments, respectively, optimized for two time windows.

2) Arc Radius Estimation (ARE) Approach: Different from the LSF approach, this approach directly estimates the arc radius of a trajectory. A circular arc can be fitted to a phase-plane trajectory segment connecting points $(x(t_1), y(t_1))$ and $(x(t_2), y(t_2))$, whose circular center is assumed to be $(x_0, 0)$. x_0 and radius $r(t)$ for that segment can be solved as follows. Here, $y(t)$ could be either simply equal to $x'(t)$ or $x'(t)/\lambda$ as described by (14):

$$[x(t_1) - x_0]^2 + y^2(t_1) = [x(t_2) - x_0]^2 + y^2(t_2) \tag{17}$$

$$x_0 = \frac{x(t_1) + x(t_2)}{2} + \frac{y^2(t_2) - y^2(t_1)}{2\cdot[x(t_2) - x(t_1)]} \tag{18}$$

$$r(t) \approx \sqrt{[x(t_1) - x_0]^2 + y^2(t_1)}, t = [t_1, t_2]. \tag{19}$$

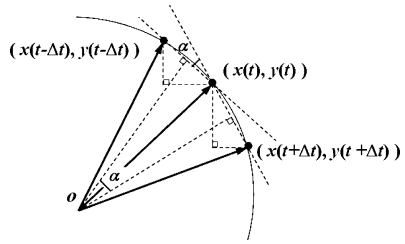

Fig. 4. Calculation of ω.

If $y(t) = x'(t)$, it is not necessary to estimateλ, but the resulted estimates of time series $r(t)$ will have large swings around angular frequency ω_d, especially when the values of $x'(t)$ and $x(t)$ are in obviously different scales (i.e., λ is not close to 1). Those swings do not mean actual sizes of swings in $r(t)$ and can be filtered out by a band-stop filter cover frequency ω_d. Even if $y(t) = x'(t)/\lambda$, the estimated curve of $r(t)$ has spikes due to the errors in the circular arc fitting, which can be smoothed by a low-pass filter. Compared with the LSF approach, the ARE approach is simpler but needs filters to smooth its results.

D. Estimation of Angular Velocity ω

To estimate $\omega(t)$ for the phase-plane trajectory over a time window, first scale $x'(t)$ by $1/\lambda$ to calculate $y(t)$, and then divide the resulted trajectory described by $x(t)$ and $y(t)$ into short arcs for intervals of Δt. As shown in Fig. 4, $\omega(t)$ at point $(x(t), y(t))$ can be calculated using the preceding and succeeding arcs, respectively, connected with points $(x(t-\Delta t), y(t-\Delta t))$ and $(x(t+\Delta t), y(t+\Delta t))$. The two arcs have approximately the same circular center as indicated by "o" and the same center angle α. From Fig. 4, $\alpha(t)$ and $\omega(t)$ can be calculated at intervals of Δt :

$$\alpha(t) = \left|\arctan\left(\frac{|y(t+\Delta t) - y(t)|}{|x(t+\Delta t) - x(t)|}\right) - \arctan\left(\frac{|y(t) - y(t-\Delta t)|}{|x(t) - x(t-\Delta t)|}\right)\right| \tag{20}$$

$$\omega(t) = \alpha(t)/\Delta t. \tag{21}$$

E. Calculation of Stability Margin

The segment $h(r)(r < r_m)$ estimated using measurement data over a time window does not contain boundary point (r_M, h_M) unless the system loses stability. A smooth (differentiable) function can be fitted to that segment to extrapolate (r_M, h_M). This paper uses polynomial extrapolation as an example to study the feasibility of estimating (r_M, h_M) before it is reached. Other extrapolation techniques might be studied in future work. Consider an n-degree polynomial passing through the origin:

$$h = \sum_{i=1}^{n} a_i r^i. \tag{22}$$

Solve a_i to make the polynomial optimally fit $h(r)(r < r_m)$ in a least-square sense, and then estimate (r_M, h_M) by finding the closest local maximum of $h(r)$, i.e., minimizing r with $h' = 0$ and $h'' < 0$. In general, a higher-degree polynomial can fit better the $h(r)$ for a more complex system but tends to estimate

(r_M, h_M) closer to the bottom point due to the over-fitting issue. As a result, the stability margin will be estimated more pessimistically. Simulations indicate that a degree between 5 and 8 is recommended depending on the complexity of the studied system. In the case studies below, the two-generator and 179-bus systems, respectively, adopt degrees 5 and 8.

In fact, the closer the ball has been to the boundary, the more accurate the estimated r_M will be. If the system over the current time window has sufficient stability margin (i.e., the ball is around the surface's bottom and far away from the boundary), r_M might not be extrapolated well. Especially if the $h(r)$ segment from measurements does not have an obvious inflection point, r_M might be estimated too big. Here, an "obvious inflection point" means a point where $h'' = 0$ but h' is credibly positive (exceeding the size of its error estimate). However, it should be noted that the method proposed in this paper is focused on situational awareness for system status already approaching the edge of stability (i.e., the ball has been close to the boundary). Therefore, it does not hurt to set an upper limit r^* for the estimates of r_M according to the acceptable maximum deviation of the monitored variable, e.g., 0.3 p.u. for a bus voltage magnitude.

The vertical and horizon distances from the ball's location (r, h) to estimated (r_M, h_M) indicate the stability margins of the system, respectively, in terms of r and h. A better-defined stability margin index should give considerations to the ball's mechanical energy composed of kinetic energy E_K and potential energy E_P :

$$E_K = m(v^2 + \omega^2 r^2)/2 \tag{23}$$

$$E_P = mgh. \tag{24}$$

If friction is ignored (resulting in slightly more conservative stability margins), the ball will not reach (r_M, h_M) if its mechanical energy is less than the maximum potential energy:

$$\begin{aligned} E_K + E_P &= m(v^2 + \omega^2 r^2)/2 + mgh \\ &\le E_{P,\max} = mgh_M. \end{aligned} \tag{25}$$

Accordingly, define an instability risk index (IRI), indicating the risk of the system losing stability, shown in (26) at the bottom of the page. Define a percentage stability margin index (SMI):

$$\text{SMI} = 100\% - \text{IRI}. \tag{27}$$

Finally, Fig. 5 gives the flow chart of the method proposed in this section. The method can be applied to monitor transient stability for local variables or a wide area by means of high-sampling-rate measurements. For the former, synchronized phasor measurements are not required. For the latter, synchronized phasor measurements should be available to compute a wide-area variable/index, e.g., average frequency over a region or angle/frequency difference between generators from two interconnected regions. The estimated IRI and SMI can be online displayed together with their values in a past time window to help system operators at the control center online monitor the trend of system stability. Also, r and r_M (or h and h_M) can be displayed together to indicate how the stability margin changes under disturbances.

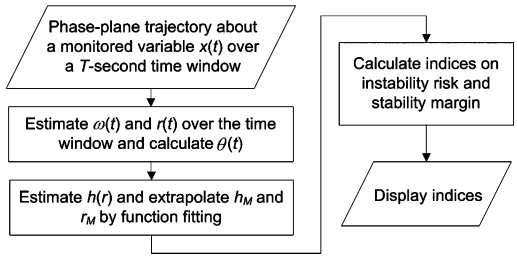

Fig. 5. Flow chart of the proposed method.

III. Case Studies

This section performs case studies on the two-generator system in Fig. 1 and a 179-bus system to validate the idea of using the proposed BOCS system to estimate stability margin and study the potentials of the method in local and wide-area applications. Dynamics behaviors of the two power systems under a series of disturbances are simulated to generate assumed continuous measurements of monitored variables.

A. Two-Generator Power System

Four temporary three-phase faults are added to bus 1 at 10 s interval, respectively, lasting 0.10 s, 0.15 s, 0.20 s, and 0.25 s. No line is tripped under those disturbances, so the system does not change its operating condition. The system loses stability after fault 4, as shown by the frequency and angle differences in Fig. 6, which are assumed to be measurements and fed to the proposed method to calculate indices IRI and SMI. Whether the final instability around $t = 30$ s is predictable will also be studied. Starting from $t = 0$ s, the method is performed every 5 s (i.e., the time window for updating the BOCS system) on the frequency and angle difference data with $r^* = 3$ Hz and 180°, respectively.

Fig. 7 gives three 5-s trajectories about frequency difference f_{12} following faults 1–3. Although the system does not lose stability, increasing swings indicate the trend toward exceeding its stability margin. The LSF and ARE approaches are both applied to estimate $r(t)$. The dashed lines in Fig. 7 indicate the optimal logarithmic spirals fitting three trajectories. Fig. 8 compares the estimates of $r(t)$ from two approaches, which basically match each other. The $r(t)$ from the LSF approach is smooth and is adopted to estimate $h(r)$. Fig. 8 also indicates the estimated r_M by dashed lines.

$h(r)$ for each time window can be estimated by (8)–(10). g may either take a constant or be calculated by (4) for each time window. For example, for the time window following fault 3, $g_0 = 374.85$. To study how g may impact the estimation of $h(r)$, Fig. 9 compares the estimates of $h(r)$ for $g = g_0/2, g = g_0$

$$\text{IRI} = \begin{cases} \frac{E_K + E_P}{E_{P,\max}} \times 100\% = \left(\frac{h}{h_M} + \frac{v^2 + \omega^2 r^2}{2gh_M}\right) \times 100\%, & \text{if } r_M < r^* \\ \frac{r}{r^*} \times 100\%, & \text{otherwise} \end{cases} \tag{26}$$

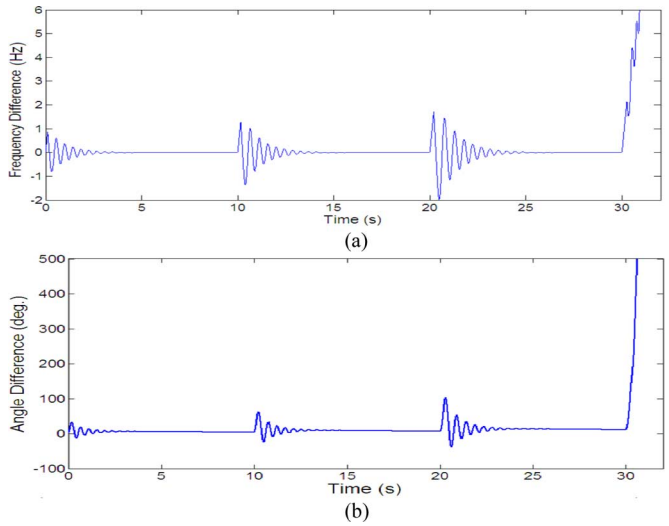

Fig. 6. System dynamics under four temporary faults. (a) Frequency difference between two generators. (b) Angle difference between two generators.

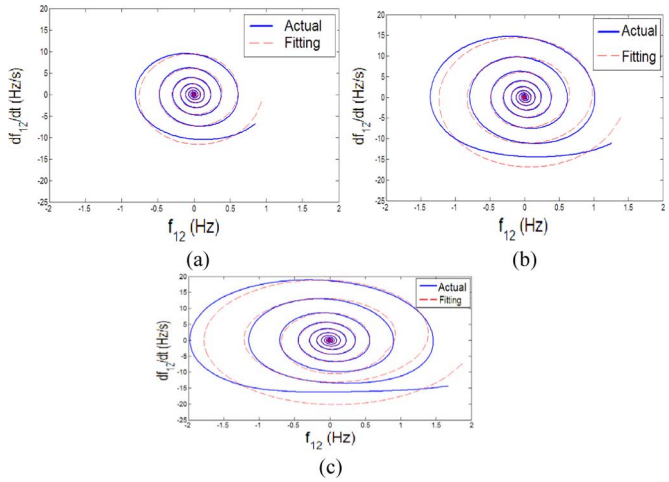

Fig. 7. Phase-plane trajectories (five seconds) following faults 1–3. (a) After fault 1. (b) After fault 2. (c) After fault 3.

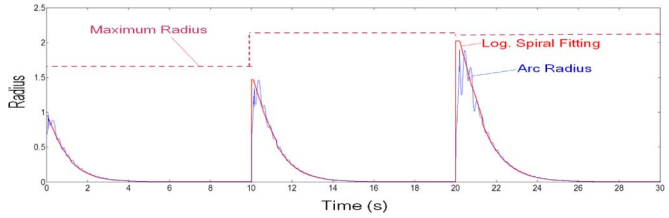

Fig. 8. Radius for the frequency difference.

and $g = 2g_0$. The resulted $h(r)$ curves have the same pattern except for their scales in h. They all have one stationary point at the origin and another around $r = 2$ (Hz), i.e., boundary point (r_M, h_M). From Fig. 9, the value of g does not influence the prediction of the ball approaching or reaching the boundary point.

For the convenience of comparing the $h(r)$ curves estimated for the three time windows following faults 1–3, let $g = 1000$ in this case study. The results are shown by solid lines in Fig. 10, where each "o" indicates the highest location the ball has reached over the time window. Because, for this case, the operating condition never changes, three $h(r)$ curves match well. Fit polynomial functions of degree 5 to those curves to extrapolate the boundary point. The optimal fittings are shown by dashed lines. It can be observed that the three $h(r)$ curves all have an inflection point around (0.95, 0.06). After faults 2 and 3, the ball far exceeds that point, so the resulted fittings are more reliable, from which the estimates of r_M are both around 2.1 (Hz). Fig. 8 shows $r(t)$ together with the estimates of r_M to indicate the real-time stability margin in terms of r. In order to verify the estimated 2.1 (Hz) for r_M, temporary three-phase faults with duration times from 0.2 s to 0.25 s are, respectively, added to bus 1 at $t = 0$ s and simulated. Simulation results show that the maximum value that $r(t)$ may reach without cause instability is 2.16 (Hz), which is very close to 2.1 (Hz) with error <3%. IRI is calculated by (26) and shown in Fig. 11(a). Faults 1–3 raise IRI up to 48%, 68%, and 92%, which correspond to stability margins (SMI) of 52%, 32%, and 8%. The proposed method is also applied to the angle difference data to calculate IRI as shown in Fig. 11(b), which matches Fig. 11(a).

The high risk following fault 3 indicates the system may not survive after another fault at $t = 30$ s. To attempt predicting for

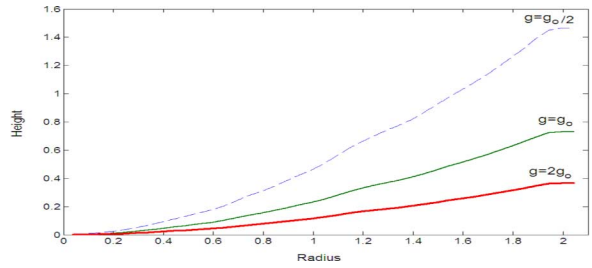

Fig. 9. $h(r)$ estimated for different g.

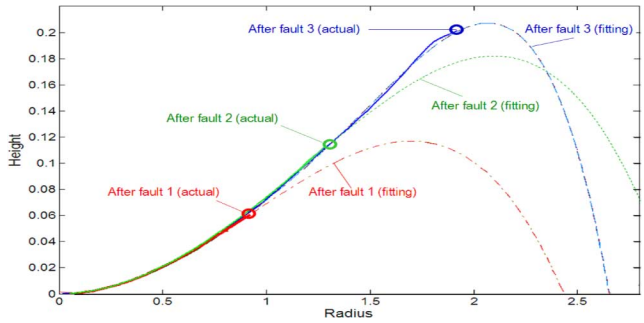

Fig. 10. $h(r)$ estimated after each fault.

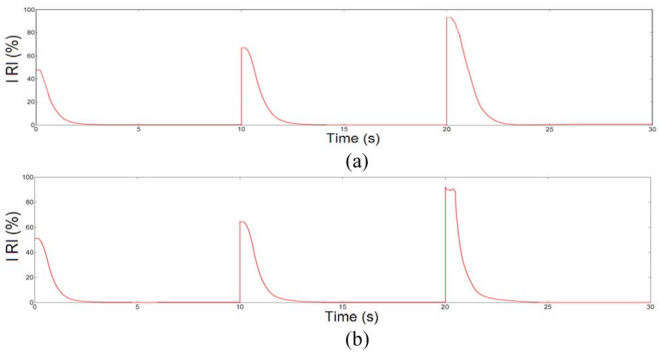

Fig. 11. Instability risk index. (a) Estimated from frequency difference data. (b) Estimated from angle difference data.

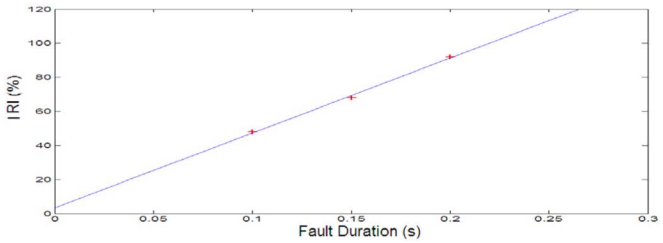

Fig. 12. Fault duration versus IRI.

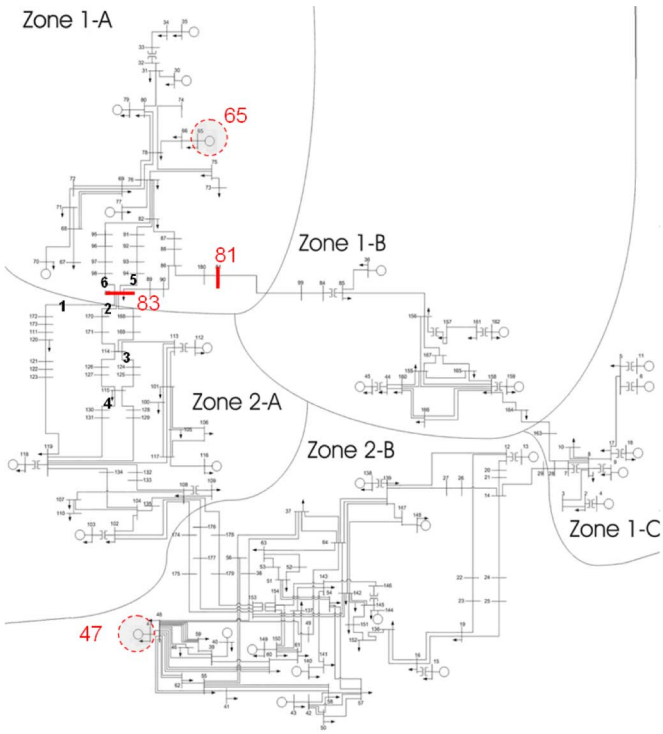

Fig. 13. The 179-bus system.

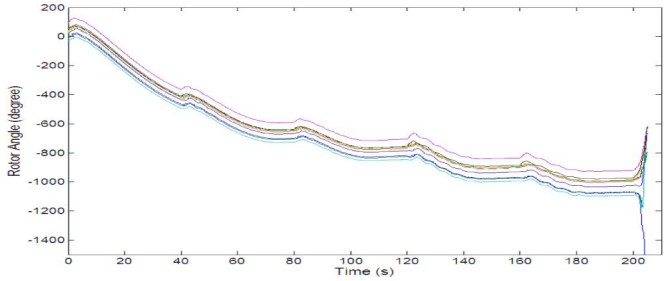

Fig. 14. Rotor angles of nine big generators.

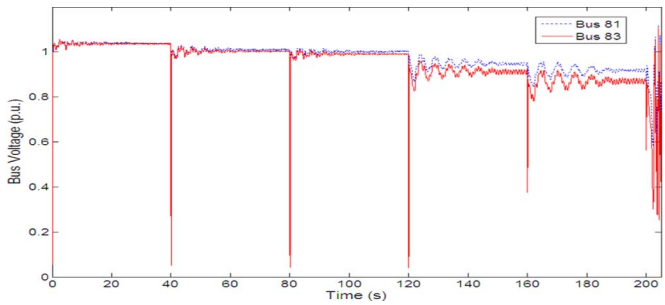

Fig. 15. Voltage magnitudes at buses 81 and 83.

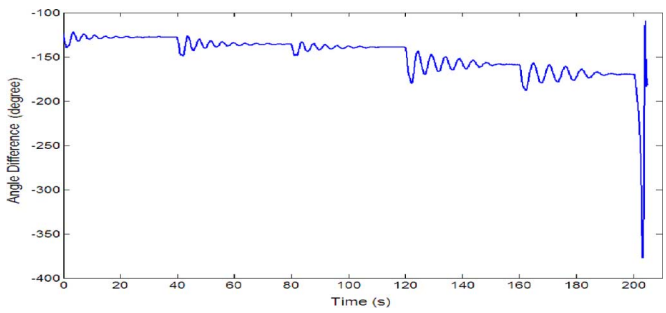

Fig. 16. Rotor angle difference between generators 47 and 65.

what duration time a fault at $t = 30$ s may cause instability, the relationship between the fault duration and IRI for faults 1–3 is studied by Fig. 12, where the three points are determined by three fault durations and three maxima of IRI and are fitted by a straight line. It is learned from that straight line that $\text{IRI} > 100\%$ if the fault $\text{duration} > 0.22$ s. Additional simulations prove that a fault at $t = 30$ s lasting longer than 0.23 s will cause instability, which matches the guessed 0.22 s well.

This case study validates the idea of the proposed method, i.e., stability margin can directly be estimated from phase-plane trajectories by means of the proposed adaptive power system equivalent—BOCS system.

B. The 179-Bus Power System

To study the potentials of the proposed method on estimating stability margins for wide-area stability problems, it is tested on the 179-bus system as shown in Fig. 13. The system is a simplified WECC ac transmission system. The interface at bus 83 between Zone 1-A and Zone 2-A corresponds to the California-Oregon Intertie of the WECC system, which was involved in the Western cascading and separation event on July 2, 1996 [11].

In this case study, system collapse at that interface is created by adding six permanent three-phase faults at intervals of 40 s. Fig. 13 indicates the locations and order of the faults by numbers 1–6. Each fault lasts 0.1 s and is cleared by opening the fault line. They increasingly weaken the interface but do not break its connection. The system loses angular stability right after fault 6 as shown in Fig. 14. Fast voltage collapse can also be detected at bus 83 and some other nearby buses. Fig. 15 shows voltage collapse at buses 83 and 81 by their voltage magnitudes V_{83} and V_{81}. Bus 81 is actually at another interface, i.e., between Zone 1-A and Zone 1-B. Fig. 16 shows the angle difference $\delta_{47,65}$ between generators 47 and 65, which are, respectively, located in the north Zone 1-A and south Zone 2-B.

The proposed method is respectively performed on

- individual V_{83} and V_{81} (no need of synchronized phasor measurements);
- $\delta_{47,65}$ (calculated by synchronized phasor measurements at generators 47 and 65).

Different from the previous case study, this case increasingly stresses the operating condition (weakening the topology around that interface) by a series of permanent faults. Thus, the steady-state values of monitored variables might be changed.

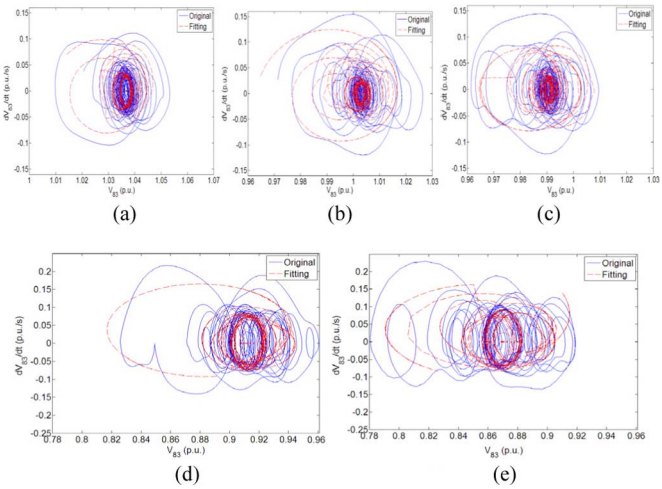

Fig. 17. The 40-s phase-plane trajectories about V_{83} following faults 1–5. (a) After fault 1. (b) After fault 2. (c) After fault 3. (d) After fault 4. (e) After fault 5.

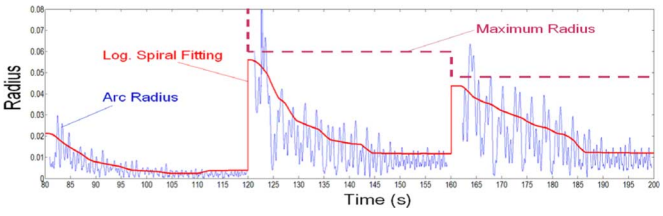

Fig. 18. Radius for V_{83}.

Fig. 17 gives five 40-s phase-plane trajectories about V_{83}, respectively, following faults 1–5. For the convenience of comparison, the first three trajectories are drawn in the same scale, and the last two trajectories adopt another different scale since they are much bigger in size. Fig. 14–16 indicate oscillations in a short period following each fault. The dominant mode has frequency around 0.25 Hz, so let $T = 10$ s. For each 10-s time window, scale the derivative of V_{83} by ratio λ calculated using (13), and estimate the logarithmic spiral optimally fitting the phase-plane trajectory. Fig. 17 gives the fitting results by the dashed lines, which are actually linked spiral segments of different parameters.

Fig. 18 shows the estimates of $r(t)$ from the LSF and ARE approaches. The result from the LSF approach is used to estimate $h(r)$. The result from the ARE approach can be fed into a low-pass filter with the cut-off frequency < 0.25 Hz to get a signal similar to that from the LSF approach.

Let $g = 1$ and $r^* = 0.3$ p.u. Following each of faults 3–5, the $h(r)$ curves estimated from phase-plane trajectories are shown by solid lines in Fig. 19, where each "o" indicates the highest locations the ball has reached. Since the operating condition is increasingly stressed, three $h(r)$ curves indicate a trend that the concave surface becomes vertically flattened and horizontally shrunk. Fit a polynomial function of degree 8 to each curve to extrapolate the boundary point. After fault 3, the ball does not reach an obvious inflection point, so the estimated $r_M > r*$. This means that the system has still sufficient stability margin. After faults 4 and 5, the boundary points are, respectively, estimated at (0.059, 0.031) and (0.045, 0.017). Fig. 18 shows $r(t)$ and the estimated r_M together. Fig. 20 gives the IRI calculated

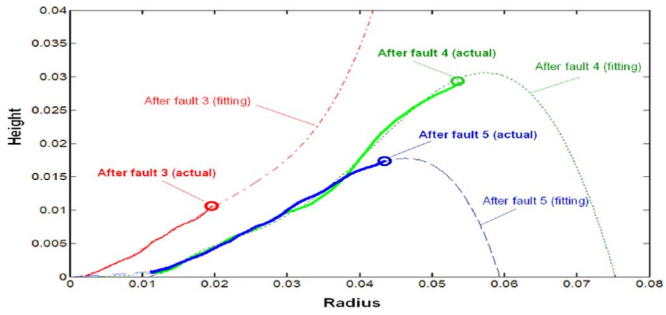

Fig. 19. $h(r)$ estimated for V_{83} after faults 3–5.

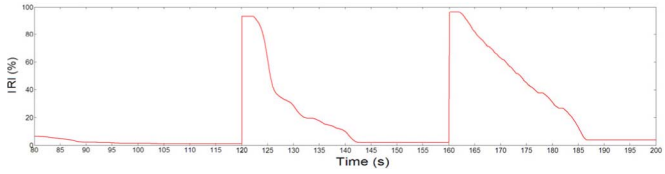

Fig. 20. Instability risk index for V_{83} after faults 4 and 5.

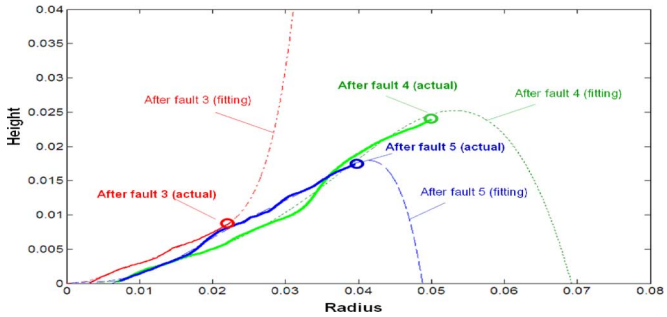

Fig. 21. $h(r)$ estimated for V_{81} after faults 3–5.

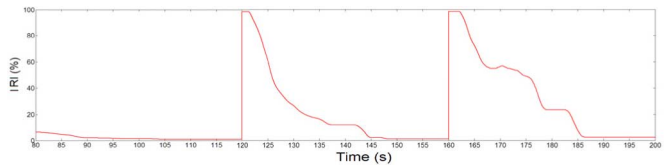

Fig. 22. Instability risk index for V_{81} after faults 4 and 5.

after faults 3–5. It is lower than 10% (i.e., SMI $> 90\%$) after fault 3 but has two peaks exceeding 90% (i.e., SMI $< 10\%$) after faults 4 and 5.

Still let $g = 1$ and $r^* = 0.3$ p.u. The method is then performed on V_{81} to obtain Figs. 21 and 22, which indicate the same trend as for V_{83}. The test results on V_{83} and V_{81} indicate such a finding: when a power system is going to collapse at an interface, different system variables near that interface may have similar dynamics patterns, indicating decreasing stability margin. Thus, the proposed method has potentials to online indicate the trend toward instability by real-time high-sampling-rate measurements about strategically selected variables. It is also noticed that synchronized phasor measurements are unnecessary for this case because the monitored V_{83} and V_{81} are either at or close to the interface that is involved in instability.

To benchmark with the results from synchronized phasor measurements, the method is also tested on $\delta_{47,65}$ with $g = 300$

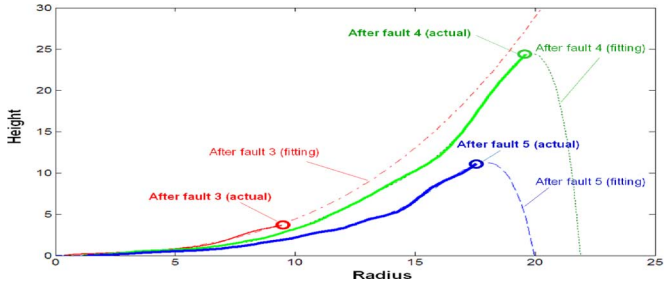

Fig. 23. $h(r)$ estimated for $\delta_{47,65}$ after faults 3–5.

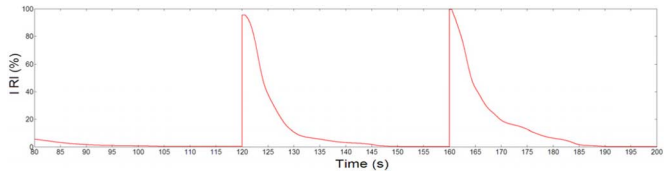

Fig. 24. Instability risk index for $\delta_{47,65}$ after faults 4 and 5.

and $r^* = 180°$. The results are given in Figs. 23 and 24, which indicate the same trend for V_{83} and V_{81}.

IV. Conclusion

This paper presents a novel method for real-time estimation of power system stability margin. The method is based on an adaptive power system equivalent—BOCS system, which represents the dynamics behavior of a monitored variable under disturbances. The parameters of the BOCS system are adaptive to the operating condition and online identified using high-sampling-rate measurement data by means of the phase-plane trajectory of the monitored variable. Then, stability margin can directly be estimated from the BOCS system. Application of high-sampling-rate data taken at proper locations is a key because those data can authentically present real-time system dynamics, e.g., by phase-plane trajectories about the concerned stability problem. This paper aims at building a quantitative relationship between key parameters of a phase-plane trajectory and real-time stability margin. By means of that relationship, the proposed method can online indicate the trend of either decreasing stability margin due to disturbances or increasing stability margin thanks to mitigation measures. With synchronized phasor measurements available, the method also has potentials in monitoring wide-area stability for interconnected power systems. This paper has presented a new idea for using real-time high-sampling-rate measurements to develop and identify a power system's adaptive equivalent as a basis for online instability prediction. Case studies have validated that idea and demonstrated the performance of the proposed method. Implementation issues with the method on actual large-scale power systems will be addressed by future work. Moreover, other types of adaptive power system equivalents (e.g., electrical systems rather than mechanics systems), which can be designed better for complex power systems, might be studied in the future.

References

[1] J. Bertsch, C. Carnal, D. Karlsson, J. Mcdaniel, and K. Vu, "Wide-area protection and power system utilization," *Proc. IEEE*, vol. 93, no. 5, pp. 997–1003, May 2005.

[2] S. Rovnyak, S. Kretsinger, J. Thorp, and D. Brown, "Decision trees for real-time transient stability prediction," *IEEE Trans. Power Syst.*, vol. 9, no. 3, pp. 1417–1426, Aug. 1994.

[3] K. Sun *et al.*, "An online dynamic security assessment scheme using phasor measurements and decision trees," *IEEE Trans. Power Syst.*, vol. 22, no. 4, pp. 1935–1943, Nov. 2007.

[4] R. Diao *et al.*, "Decision tree assisted controlled islanding for preventing cascading events," in *Proc. IEEE PES Power Systems Conf. Expo. (PSCE)*, 2009.

[5] J. Ma *et al.*, "Use multi-dimensional ellipsoid to monitor dynamic behavior of power systems based on PMU measurement," in *Proc. IEEE PES General Meeting*, 2008.

[6] N. Kakimoto, M. Sugumi, T. Makino, and K. Tomiyama, "Monitoring of inter-area oscillation mode by synchronized phasor measurement," *IEEE Trans. Power Syst.*, vol. 21, no. 1, pp. 260–268, Feb. 2006.

[7] J. Quintero, G. Liu, and V. Venkatasubramanian, "An oscillation monitoring system for real-time detection of small-signal instability in large electric power systems," in *Proc. IEEE PES General Meeting*, 2007.

[8] A. R. Messina *et al.*, "Interpretation and visualization of wide-area PMU measurements using Hilbert analysis," *IEEE Trans. Power Syst.*, vol. 21, no. 4, pp. 1763–1771, Nov. 2006.

[9] K. Sun and S. Lee, "Power system security pattern recognition based on phase space visualization," in *Proc. IEEE Int. Conf. Electric Utility Deregulation and Restructuring and Power Technologies (DRPT 2008)*, Nanjing, China, Apr. 2008.

[10] S. K. Mishra, Fitting a Logarithmic Spiral to Empirical Data With Displaced Origin, Apr. 20, 2006. [Online]. Available: http://ssrn.com/abstract=897863.

[11] C. W. Taylor and D. C. Erickson, "Recording and analyzing the July 2 cascading outage [Western USA power system]," *IEEE Comput. Applicat. Power*, vol. 10, no. 1, pp. 26–30, Jan. 1997.

Kai Sun (M'06) received the B.S. degree in automation and the Ph.D. degree in control science and engineering from Tsinghua University, Beijing, China, in 1999 and 2004, respectively.

He was a postdoctoral fellow at the University of Western Ontario, London, ON, Canada, and a postdoctoral research associate at Arizona State University, Tempe, from 2005 to 2007. He is currently a project manager at EPRI, Palo Alto, CA.

Stephen T. Lee (M'69–SM'75) received the S.B., S.M., E.E., and Ph.D. degrees from the Massachusetts Institute of Technology, Cambridge, in electrical engineering, majoring in power system engineering, in 1969, 1970, 1971, and 1972, respectively.

He is Senior Technical Executive, Power Delivery and Utilization, in EPRI, Palo Alto, CA. He has over 40 years of electric power industry experience. He worked for Stone & Webster Engineering Corporation in Boston and Systems Control, Inc. in California, and he was Vice President of Consulting for Energy Management Associates (EMA). Before joining EPRI in 1998, he was an independent Consultant in utility planning and operation. At EPRI, he has been involved with technical research programs for power system analysis as well as planning and operations, and he has been actively developing new concepts and tools for power system operation and probabilistic transmission planning.

Pei Zhang (M'00–SM'05) received the Ph.D. degree from Imperial College of Science, Technology, and Medicine, University of London, London, U.K.

He is the Program Manager responsible for the Grid Operation and Planning area at EPRI, Palo Alto, CA. His current research interests include power system stability and control, reliability and security assessment, and wide-area special protection schemes.